

Supporting Information

**Self-Assembly of Dinitrosyl Iron Units into Imidazolate-Edge-Bridged Molecular Squares:
Characterization Including Mössbauer Spectroscopy**

Jennifer L. Hess, Chung-Hung Hsieh, Scott M. Brothers,
Michael B. Hall, Marcetta Y. Daresbourg*

Department of Chemistry, Texas A&M University, College Station, TX 77843

*marcetta@chem.tamu.edu

SI Table of Contents		Page #
1. IR spectra monitoring formation of complex 3: Figure S1		S2
2. ^1H NMR analysis of complex 3: Figure S2		S3
3. Mass spectral analysis of complex 3: Figure S3		S3
4. Extended packing diagram of complex 1: Figure S4		S4
5. Extended packing diagram of complex 2: Figure S5		S4
6. Extended packing diagram of complex 3: Figure S6		S5
7. Overlay of EPR spectra of complex 1: Figure S7		S6
8. Solid state and solution IR spectra of complex 3: Figure S8		S6
9. Cyclic and square-wave voltammograms for complexes 1-3: Figure S9		S7
10. Cyclic voltammograms of two reference complexes: Figure S10		S7
11. Additional computational details: Figures S10-S14, Table S1		S8
12. Full X-ray Structure Data and Tables for Complex 3		S13
13. Full Reference 32		S17

- = Complex **3**
- = (Imid-benz)(CO)Fe(NO)₂
- ▲ = assigned as hydrogen bonds of H₂O

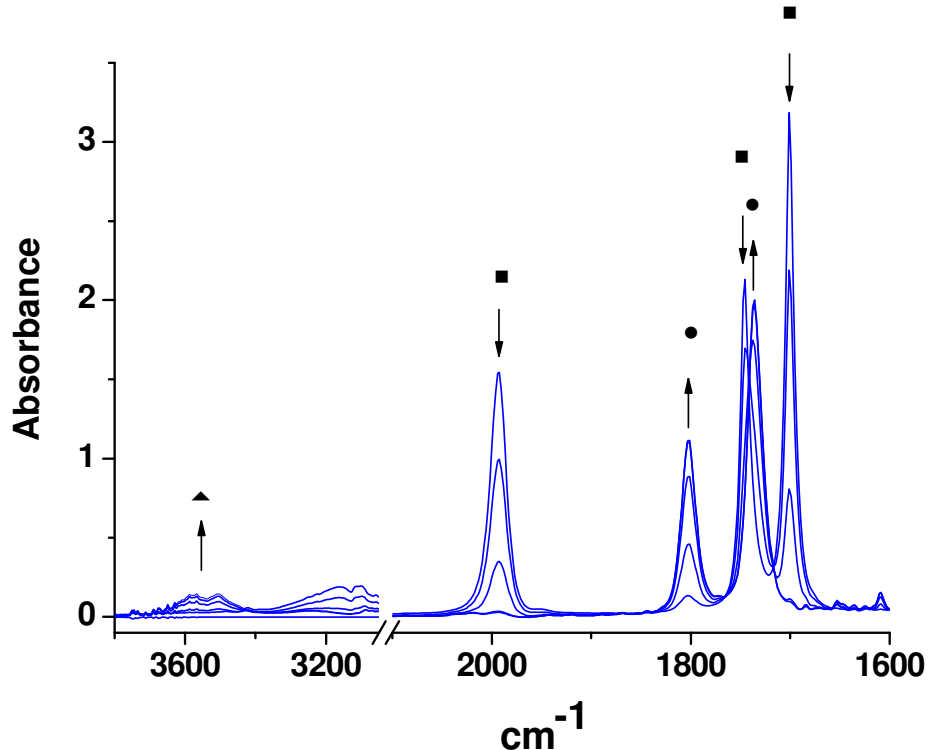
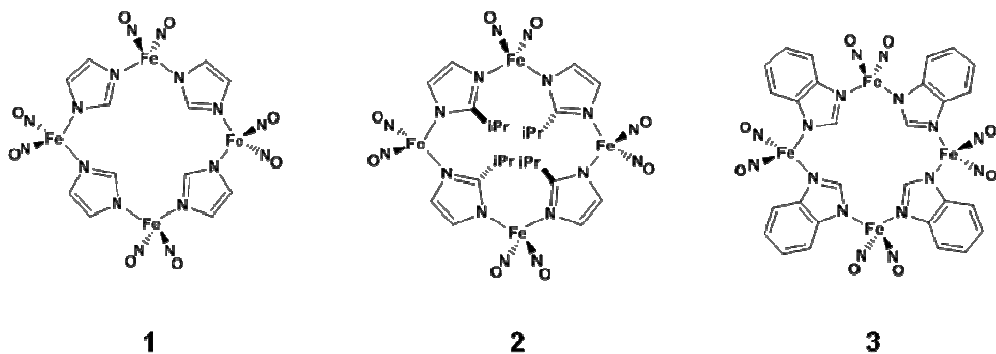


Figure S1. IR spectra demonstrating a decrease in IR bands associated with (Imid-benz)Fe(NO)₂ (initially formed upon reaction of Fe(CO)₂(NO)₂ with benzimidazole) with concomitant increase in the IR bands associated with complex **3**, indicating formation of complex **3**. Water ($\nu \sim 3500 \text{ cm}^{-1}$) was detected as a byproduct upon deliberate addition of dry O₂ to the reaction mixture.

ChemDraw Representations of Complexes **1-3**.



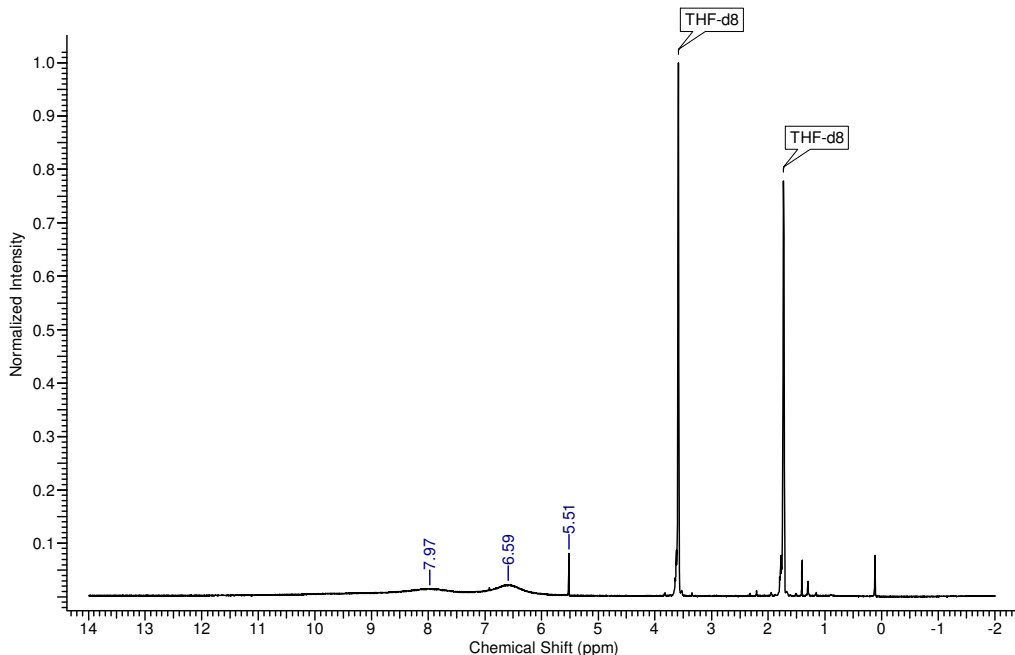


Figure S2. ¹H NMR spectrum of paramagnetic complex **3** in d-THF.

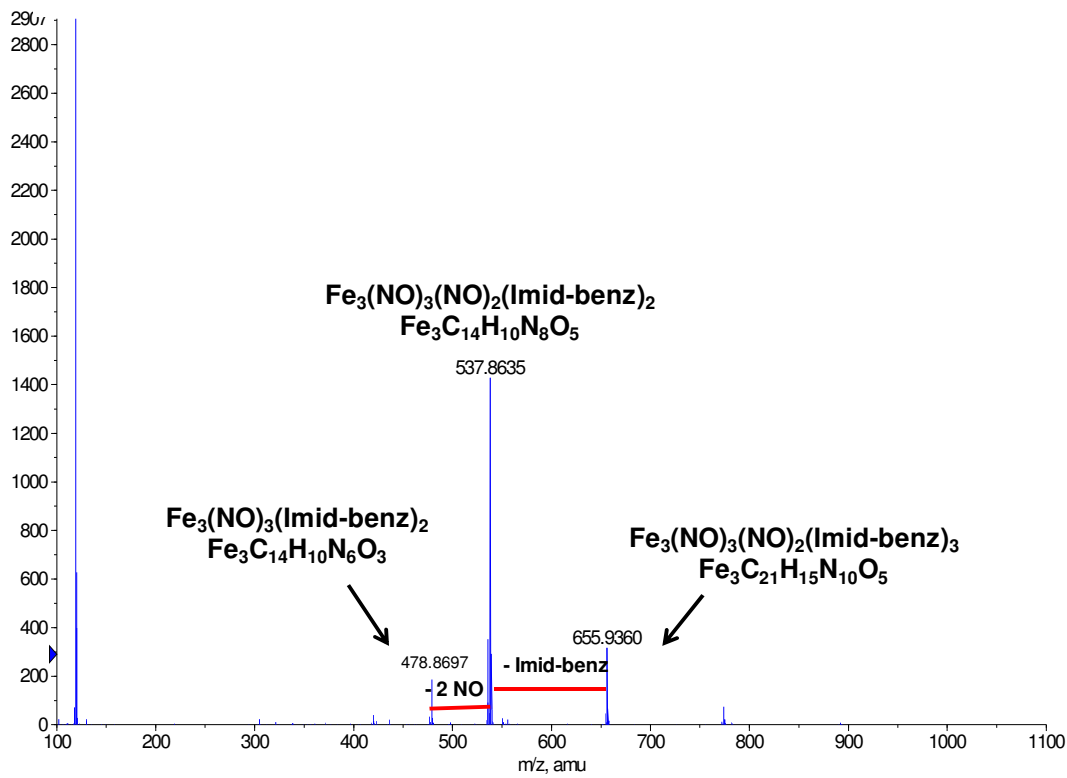


Figure S3. Full Nano-(+)-ESI mass spectrum of complex **3** with analysis of isotope bundles corresponding to fragments of the parent complex.

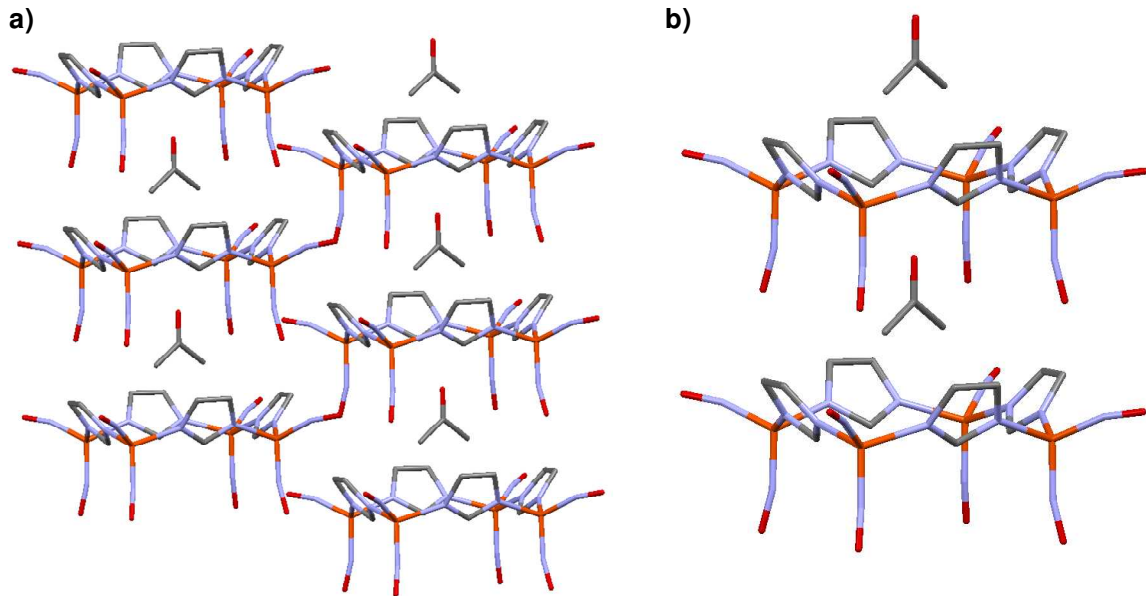


Figure S4. Two views of extended packing diagram of complex **1**.

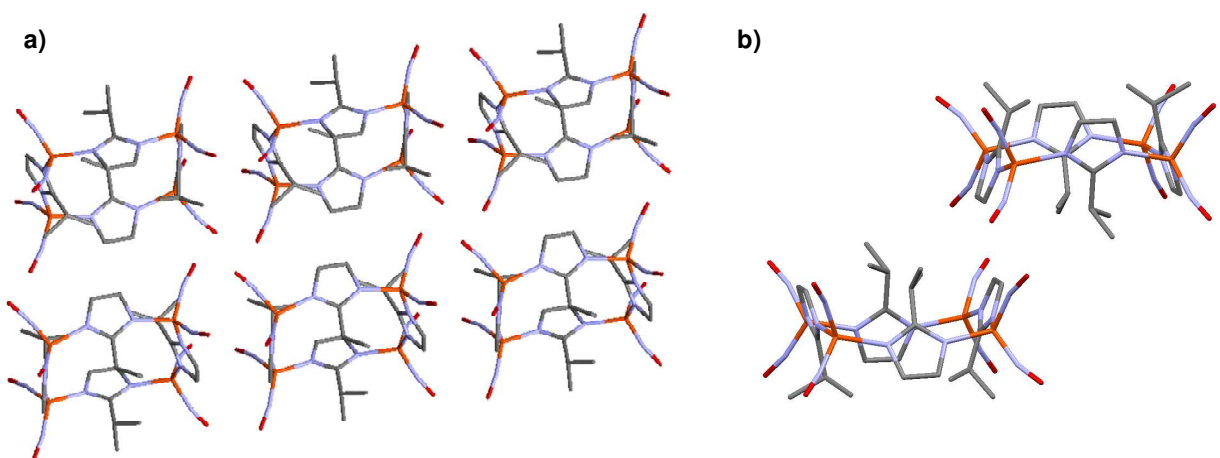


Figure S5. Two views of extended packing diagram of complex **2**.

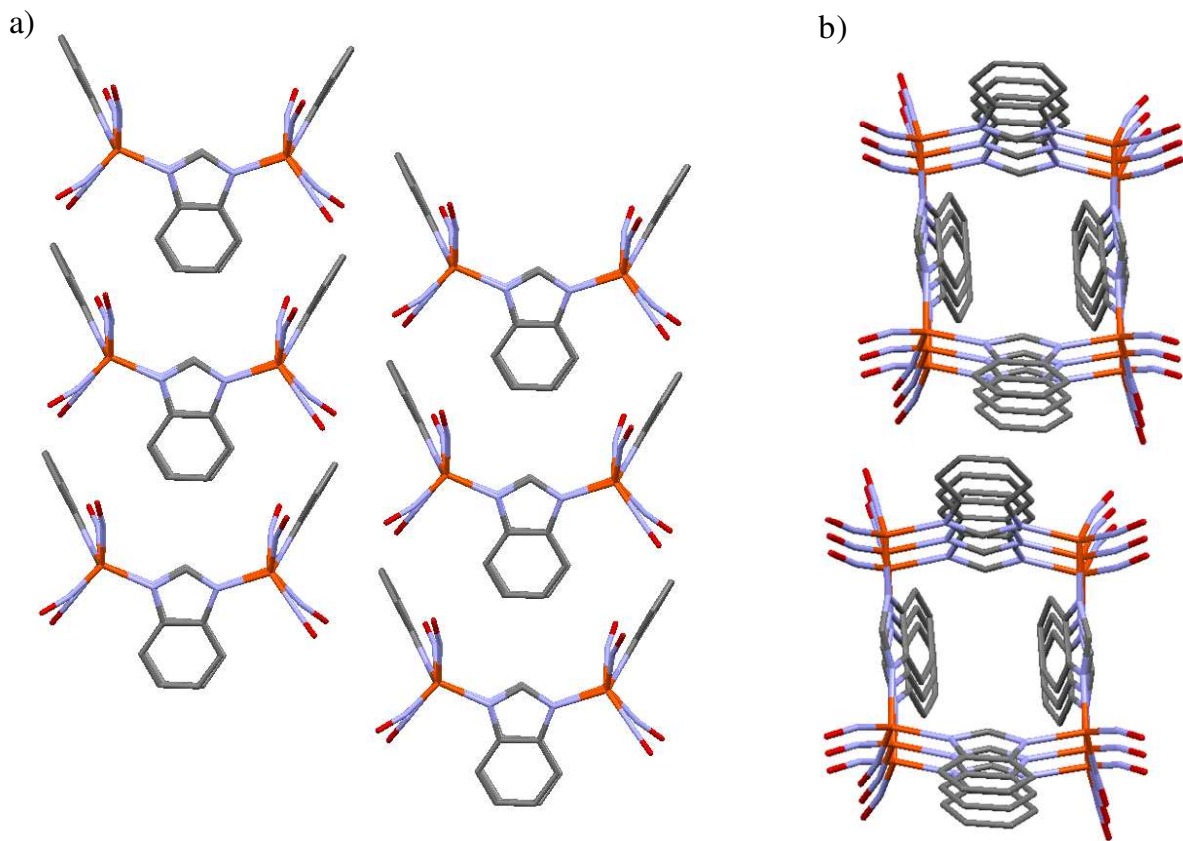


Figure S6. Two views of extended packing diagram of complex 3.

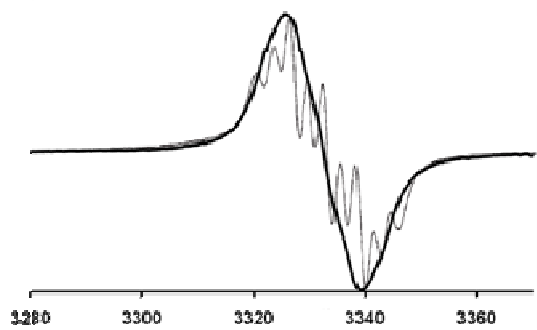


Figure S7. Overlay of Li, *et al.* spectrum of complex **1** in THF at 170 K (line width = 13 G)¹ with spectrum of complex **1** in THF at 298 K (line width = 14 G).

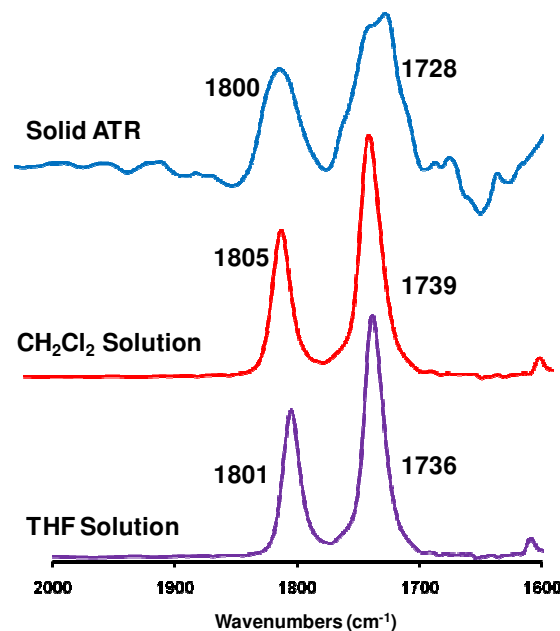


Figure S8. IR spectra of complex **3** demonstrating similar nitrosyl stretching frequencies when recorded as a solid (ATR-FTIR) and in CH₂Cl₂ and THF solutions indicating the tetramer remains intact in solution.

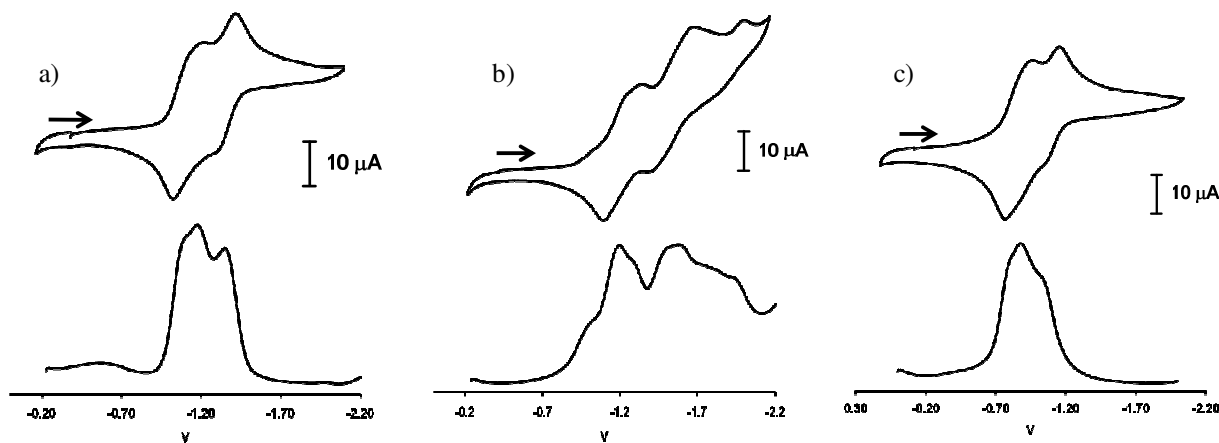


Figure S9. Cyclic and square wave voltammograms of complexes a), **1**; b), **2**; c), **3** in 2 mM CH_2Cl_2 solution. All are referenced to $\text{Cp}_2\text{Fe}/\text{Cp}_2\text{Fe}^+$.

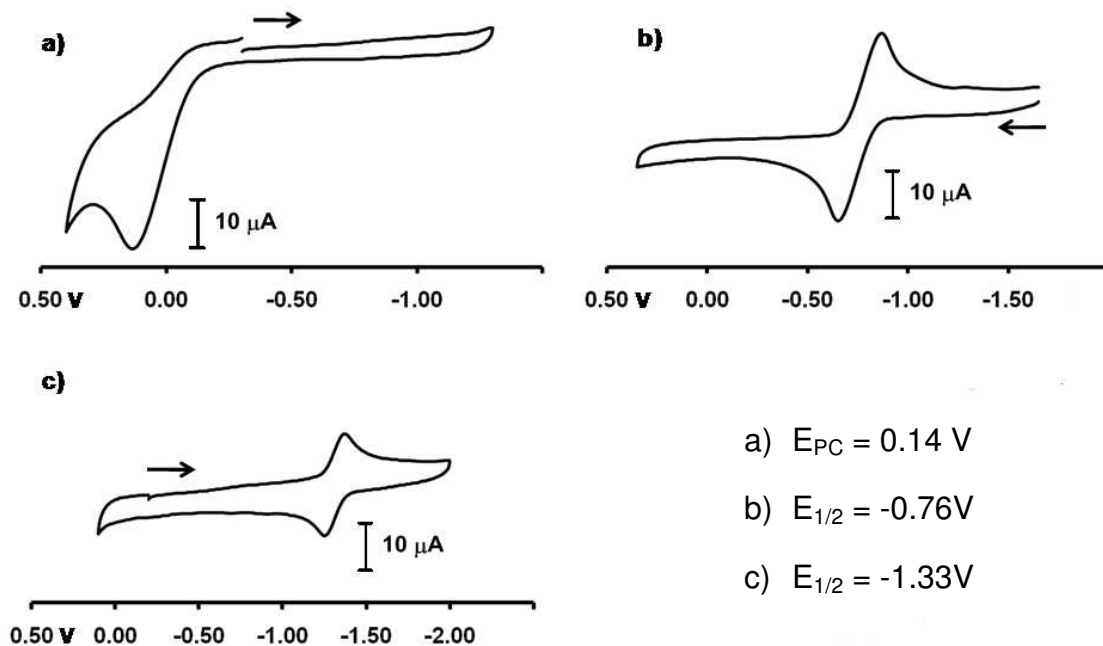


Figure S10. Cyclic voltammograms of complexes a) $(\text{NHC-}i\text{Pr})(\text{CO})\text{Fe}(\text{NO})_2$; b) $(\text{NHC-}i\text{Pr})_2\text{Fe}(\text{NO})_2$; c) $(\text{NHC-}i\text{Pr})(\text{SPh})\text{Fe}(\text{NO})_2$ in 2 mM THF solution, All are referenced to $\text{Cp}_2\text{Fe}/\text{Cp}_2\text{Fe}^+$ at scan rate 200 mV/s.¹¹

Additional Computational Details

Visualization of the frontier molecular orbitals of **1** and **3** leads to insight regarding the nature of the electronic coupling in the tetrameric systems. In both cases, despite the geometric difference between the two (up, up, up ,up vs. up, down, up, down), the character of the highest occupied molecular orbitals (the HOMO and HOMO-1 of **1** and **3_{sing.}** and the α -SOMO through α -SOMO-3 of **1** and **3_{quint.}**) display nearly identical features. The highest energy occupied orbitals are characterized by a highly delocalized superexchange pathway, as previously defined in copper-imidazolate systems described in Reference S1,¹ corresponding to the Fe₄Imid₄ unit of the tetramer, with the orbitals of the conduit corresponding to the d_{z2} atomic orbital of the iron antibonding with respect to the p _{σ} orbitals of both adjacent nitrogen atoms of the imidazolate units. The conduit is completed by an antibonding interaction of the p _{σ} orbitals of one nitrogen atom with the symmetric p _{σ} orbitals of the second nitrogen atom in an intraligand interaction. The imidazolate p _{π} ligands are not considered due to charge mismatch, similar to that of the copper imidazolate dimer.² Representative molecular orbitals responsible for the aforementioned interactions in the singlet structures can be seen in **Figure S10**.

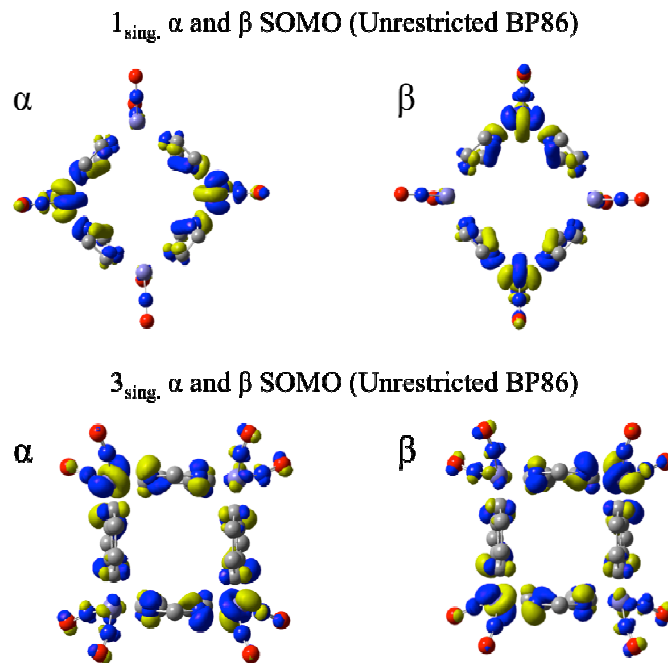


Figure S10. α and β Singly Occupied Molecular Orbitals (SOMOs) of **1_{sing.}** and **3_{sing.}**

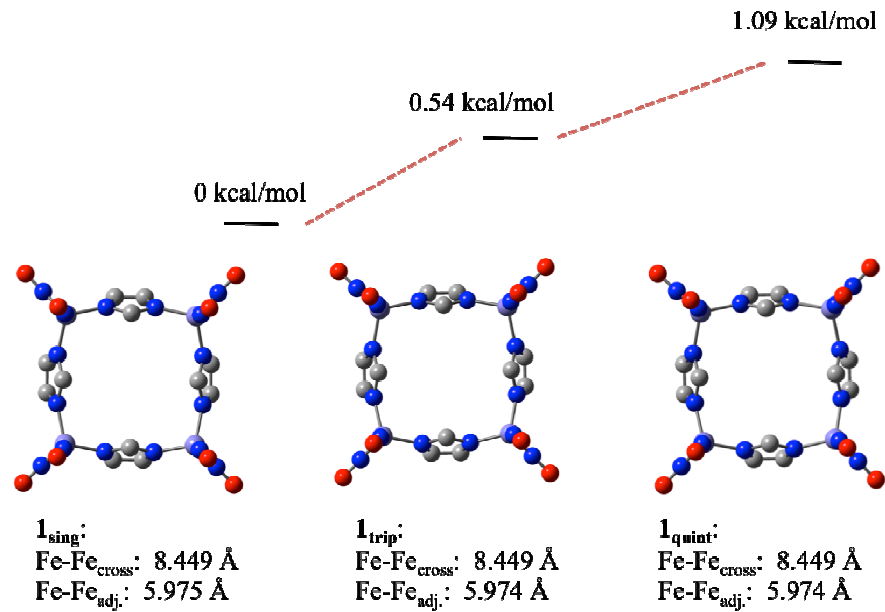


Figure S11. Isomer energy diagram of 1_{sing} , 1_{trip} ., and 1_{quint} . View is shown bisecting opposite imidazole groups through the molecular square.

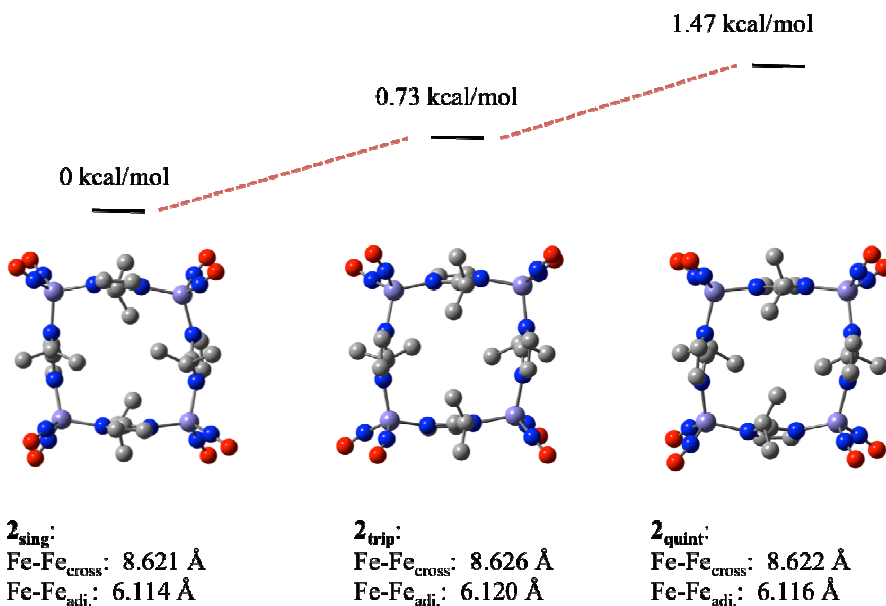


Figure S12. Isomer energy diagram of 2_{trip} . and 2_{quint} . View is shown bisecting opposite imidazole groups through the molecular square.

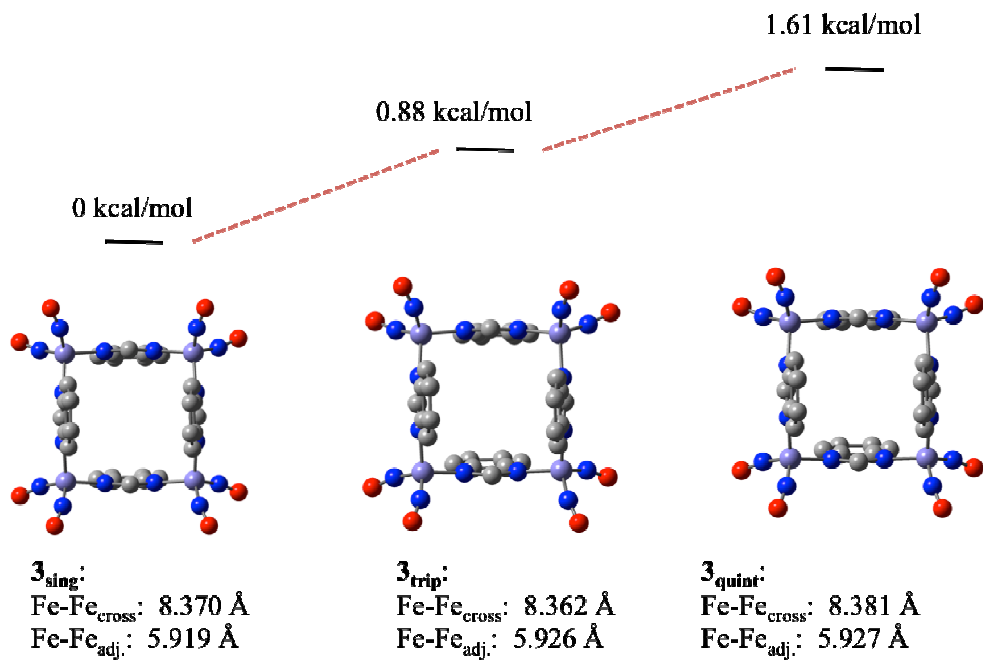


Figure S13. Isomer energy diagram of $\mathbf{3}_{\text{sing}}$, $\mathbf{3}_{\text{trip}}$, and $\mathbf{3}_{\text{quint}}$. View is shown bisecting opposite imidazole groups through the molecular square.

To further probe such solid-state effects on structure, a structure comprised of two adjacent tetramers lifted from the crystallographic unit cell was optimized with starting coordinates taken from the experimental data (**3''**). This dimer of tetramers was optimized with each tetramer in an open-shell, quintet spin state ($S = 2$). As shown in **Figure S14**, the nested (interior) imidazolates of the dimer of tetramers have arene-arene cross distances similar to the x-ray structures, while the exterior arene-arene orientations are little perturbed from the gas phase, single tetramer structure. The electronic energy of the dimer of tetramers was calculated to be 1.31 kcal/mol higher in energy than the sum of the electronic energies of two independent tetramers. This indicates that the crystal packing and nesting with close arene edge-face intermolecular distances promotes the “open, closed” structure in **3_{exp.}**; the solution- or gas-phase ground state is likely the average structure seen in **3_{calc.}**.

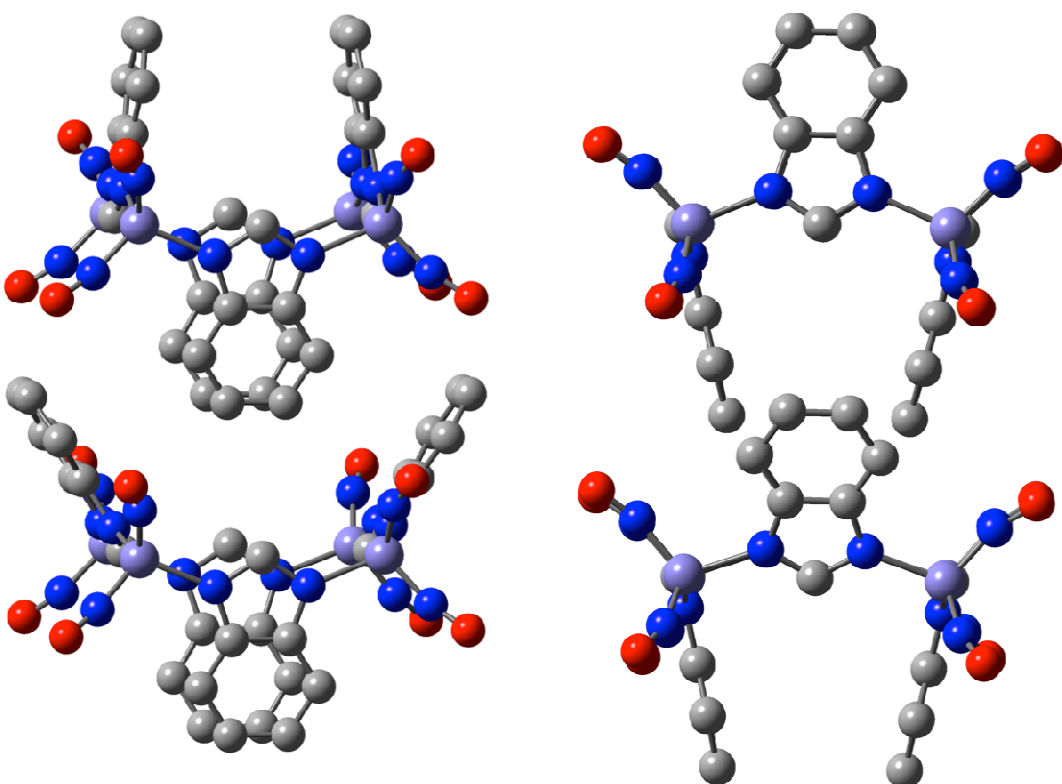


Figure S14. Two views of **3''**, which are two units of **3_{calc.}**, rotated 90° from one another.

Table S1. Selected averaged bond distances (\AA), angles ($^\circ$), and $\nu_{(\text{NO})}$ (cm^{-1}) for complexes **1**, **2**, and **3**.

	Fe-Fe _{cross}	Fe-Fe _{adj}	Imid-Imid _{cross} ^a	Fe-N-C(imid)	$\nu_{(\text{NO})}$ (cm^{-1} , CH_2Cl_2) [$\nu_{(\text{NO})}$ (cm^{-1} , g.p.)]
1_{exp}	8.440	5.971	8.425	125.33	1805, 1737
1_{quint}	8.449	5.974	7.493	126.87	1813, 1739 [1824, 1774]
1_{up/down}	8.407	5.945	5.665	126.13	
2_{exp}	8.826	6.241	7.777	133.31	1797, 1729
2_{quint}	8.624	6.118	7.079	131.22	[1807, 1759]
3_{exp}	8.520	6.027	10.240 / 3.409	127.33	1805, 1739
3_{quint}	8.371	5.924	5.419 / 5.418	124.62	1797, 1733 [1810, 1767]
3_{frozen}	8.413	5.948	10.240 / 4.776	125.06	
3_{up/up}	8.419	5.953	9.854 / 9.816	125.49	

^a Defined as the distance between opposite imidazolate groups. For **1** and **2** the value is given as the distance of opposite midpoints of imidazolate ethylene carbons, whereas for **3** the value is given as the midpoint of the carbon-carbon bond of the widest and closest points as described in Figure 3.

References:

- Wang, X.; Sundberg, E. B.; Li, L.; Kantardjieff, K. A.; Herron, S. R.; Lim, M.; Ford, P. C. *Chem. Commun.* **2005**, 477-479.
- Sun, Y.-M., Liu, C.-B.; Lin, X.-J.; Bi, S.-W. *New J. Chem.*, **2004**, 28, 270.

Table S2. Crystal data and structure refinement for [(Imid-benz)Fe(NO)₂]₄ (**3**).

Identification code	bztetra_0m
Empirical formula	C ₂₈ H ₂₀ Fe ₄ N ₁₆ O ₈
Formula weight	932.00
Temperature	110(2) K
Wavelength	0.71073 Å
Crystal system	Monoclinic
Space group	C2/c
Unit cell dimensions	a = 24.348(14) Å α = 90°. b = 7.370(4) Å β = 103.239(6)°. c = 20.786(11) Å γ = 90°.
Volume	3631(3) Å ³
Z	4
Density (calculated)	1.705 Mg/m ³
Absorption coefficient	1.638 mm ⁻¹
F(000)	1872
Crystal size	0.32 x 0.10 x 0.03 mm ³
Theta range for data collection	2.01 to 28.32°.
Index ranges	-32<=h<=31, -9<=k<=9, -27<=l<=27
Reflections collected	19482
Independent reflections	4436 [R(int) = 0.0973]
Completeness to theta = 28.32°	98.2 %
Absorption correction	Semi-empirical from equivalents
Max. and min. transmission	0.9525 and 0.6222
Refinement method	Full-matrix least-squares on F ²
Data / restraints / parameters	4436 / 0 / 253
Goodness-of-fit on F ²	1.009
Final R indices [I>2sigma(I)]	R1 = 0.0540, wR2 = 0.1256
R indices (all data)	R1 = 0.1000, wR2 = 0.1560
Largest diff. peak and hole	0.763 and -0.998 e.Å ⁻³

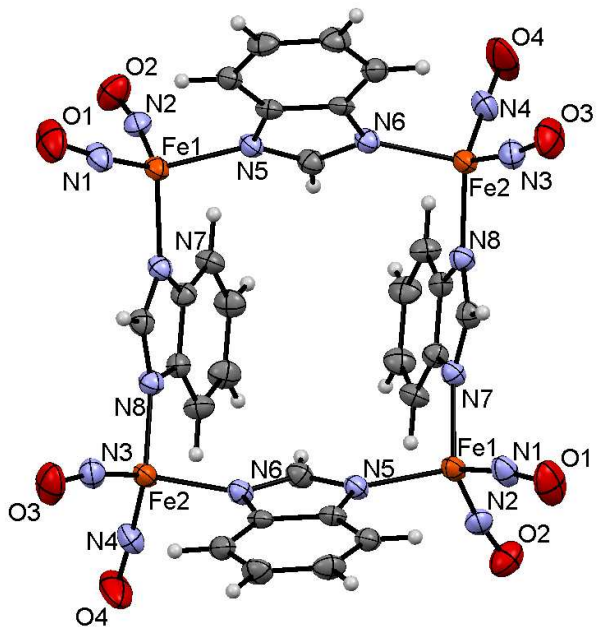


Figure S14. Thermal ellipsoid plot and labeling scheme of complex **3** with thermal ellipsoids drawn at 50 % probability.

Table S3. Bond lengths [\AA] and angles [$^\circ$] for $[(\text{Imid-benz})\text{Fe}(\text{NO})_2]_4$ (**3**).

Fe(1)-N(2)	1.690(4)
Fe(1)-N(1)	1.690(4)
Fe(1)-N(7)	2.014(4)
Fe(1)-N(5)	2.021(3)
Fe(2)-N(4)	1.678(4)
Fe(2)-N(3)	1.688(4)
Fe(2)-N(8)	1.998(4)
Fe(2)-N(6)	2.017(3)
N(1)-O(1)	1.172(5)
N(2)-O(2)	1.176(5)
N(3)-O(3)	1.170(5)
N(4)-O(4)	1.183(5)
N(5)-C(1)	1.336(5)
N(5)-C(2)	1.404(5)
N(6)-C(1)	1.349(5)
N(6)-C(3)	1.392(5)
N(7)-C(8)	1.328(5)

N(7)-C(9)	1.396(5)
N(8)-C(8)#1	1.340(5)
N(8)-C(12)	1.407(5)
C(2)-C(7)	1.393(5)
C(2)-C(3)	1.410(6)
C(3)-C(4)	1.399(5)
C(4)-C(5)	1.374(6)
C(5)-C(6)	1.411(7)
C(6)-C(7)	1.377(6)
C(8)-N(8)#1	1.340(5)
C(9)-C(12)#1	1.394(6)
C(9)-C(10)	1.397(6)
C(10)-C(11)	1.387(6)
C(11)-C(14)#1	1.394(6)
C(12)-C(9)#1	1.394(6)
C(12)-C(13)	1.394(6)
C(13)-C(14)	1.380(6)
C(14)-C(11)#1	1.394(6)
N(2)-Fe(1)-N(1)	113.10(19)
N(2)-Fe(1)-N(7)	106.63(16)
N(1)-Fe(1)-N(7)	109.69(16)
N(2)-Fe(1)-N(5)	111.99(16)
N(1)-Fe(1)-N(5)	109.20(16)
N(7)-Fe(1)-N(5)	105.95(14)
N(4)-Fe(2)-N(3)	115.20(19)
N(4)-Fe(2)-N(8)	114.00(17)
N(3)-Fe(2)-N(8)	110.27(17)
N(4)-Fe(2)-N(6)	105.03(17)
N(3)-Fe(2)-N(6)	107.52(16)
N(8)-Fe(2)-N(6)	103.81(14)
O(1)-N(1)-Fe(1)	164.1(4)
O(2)-N(2)-Fe(1)	169.1(3)
O(3)-N(3)-Fe(2)	166.7(4)
O(4)-N(4)-Fe(2)	167.8(4)
C(1)-N(5)-C(2)	104.4(3)
C(1)-N(5)-Fe(1)	126.7(3)

C(2)-N(5)-Fe(1)	128.8(3)
C(1)-N(6)-C(3)	104.1(3)
C(1)-N(6)-Fe(2)	126.8(3)
C(3)-N(6)-Fe(2)	129.1(3)
C(8)-N(7)-C(9)	105.1(3)
C(8)-N(7)-Fe(1)	128.5(3)
C(9)-N(7)-Fe(1)	126.4(3)
C(8)#1-N(8)-C(12)	104.3(3)
C(8)#1-N(8)-Fe(2)	127.0(3)
C(12)-N(8)-Fe(2)	127.8(3)
N(5)-C(1)-N(6)	115.6(4)
C(7)-C(2)-N(5)	131.1(4)
C(7)-C(2)-C(3)	121.5(4)
N(5)-C(2)-C(3)	107.5(3)
N(6)-C(3)-C(4)	130.5(4)
N(6)-C(3)-C(2)	108.4(3)
C(4)-C(3)-C(2)	121.1(4)
C(5)-C(4)-C(3)	117.1(4)
C(4)-C(5)-C(6)	121.6(4)
C(7)-C(6)-C(5)	122.0(4)
C(6)-C(7)-C(2)	116.8(4)
N(7)-C(8)-N(8)#1	115.1(4)
C(12)#1-C(9)-N(7)	107.8(3)
C(12)#1-C(9)-C(10)	121.2(4)
N(7)-C(9)-C(10)	131.0(4)
C(11)-C(10)-C(9)	116.9(4)
C(10)-C(11)-C(14)#1	121.5(4)
C(9)#1-C(12)-C(13)	121.6(4)
C(9)#1-C(12)-N(8)	107.8(3)
C(13)-C(12)-N(8)	130.6(4)
C(14)-C(13)-C(12)	116.8(4)
C(13)-C(14)-C(11)#1	122.0(4)

Symmetry transformations used to generate equivalent atoms:

#1 -x+1,y,-z+1/2

Full Reference 32.

Gaussian 09, Revision A.1, Frisch, M. J.; Trucks, G. W.; Schlegel, H. B.; Scuseria, G. E.; Robb, M. A.; Cheeseman, J. R.; Scalmani, G.; Barone, V.; Mennucci, B.; Petersson, G. A.; Nakatsuji, H.; Caricato, M.; Li, X.; Hratchian, H. P.; Izmaylov, A. F.; Bloino, J.; Zheng, G.; Sonnenberg, J. L.; Hada, M.; Ehara, M.; Toyota, K.; Fukuda, R.; Hasegawa, J.; Ishida, M.; Nakajima, T.; Honda, Y.; Kitao, O.; Nakai, H.; Vreven, T.; Montgomery, Jr., J. A.; Peralta, J. E.; Ogliaro, F.; Bearpark, M.; Heyd, J. J.; Brothers, E.; Kudin, K. N.; Staroverov, V. N.; Kobayashi, R.; Normand, J.; Raghavachari, K.; Rendell, A.; Burant, J. C.; Iyengar, S. S.; Tomasi, J.; Cossi, M.; Rega, N.; Millam, N. J.; Klene, M.; Knox, J. E.; Cross, J. B.; Bakken, V.; Adamo, C.; Jaramillo, J.; Gomperts, R.; Stratmann, R. E.; Yazyev, O.; Austin, A. J.; Cammi, R.; Pomelli, C.; Ochterski, J. W.; Martin, R. L.; Morokuma, K.; Zakrzewski, V. G.; Voth, G. A.; Salvador, P.; Dannenberg, J. J.; Dapprich, S.; Daniels, A. D.; Farkas, Ö.; Foresman, J. B.; Ortiz, J. V.; Cioslowski, J.; Fox, D. J. Gaussian, Inc., Wallingford CT, 2009.